


Influence of viscoelastic interfaces on power transmission through an elastic plate by finite piezoelectric transducers

Journal of Vibration and Control
2017, Vol. 23(7) 1193–1205
© The Author(s) 2015
Reprints and permissions:
sagepub.co.uk/journalsPermissions.nav
DOI: 10.1177/1077546315591335
journals.sagepub.com/home/jvc


Liling Tang and Feng Jin

Abstract

A finite elastic plate, partially covered by piezoelectric patches on two sides to periodically charge or recharge electronic devices operating in a sealed armor, is considered to study the effects of a viscoelastic interface on the resonant frequency, transformation ratio, efficiency, displacement and stress distributions of the structure. Based on the shear-slip model, we apply the Fourier series method to analyze the symmetric thickness-twist modes of the system containing an imperfect viscoelastic interface. An examination of the numerical results confirms the good convergence and high precision of the Fourier series method. If an appropriate thickness ratio is chosen, the energy-trapping phenomenon is well presented. The numerical results also reveal that the transformation ratio, efficiency and displacement of the system decrease for weaker interfaces, whereas the resonant frequency is not sensitive to interface damping parameters. This result could provide a theoretical guide to design high-performance piezoelectric plate transformers.

Keywords

Viscoelastic interface, piezoelectric transducer, shear-slip model, resonant frequency, energy trapping

1. Introduction

The conditions involved in powering electronic devices that operate in a sealed armor or in other hazardous environments, such as nuclear storage facilities, have led to the current interest in periodically charging and/or recharging batteries without perforating the barrier. For instance, to ensure the reliability and performance of nuclear stockpiles, piezoelectric transducers have been proposed, which generate acoustic waves that propagate through a sealed armor and transmit a small amount of power to the electronic devices inside the sealed armor. Hu et al. (2003) first examined the feasibility of this idea by investigating a transmit and receive piezoelectric transducer (Zhang et al., 2010) separated by a sealed armor (wall). This transmission device uses the direct and indirect piezoelectric effects as a means of generating stress waves that are transmitted through the walls, where the received wave is converted into an electric power using a piezoelectric and then delivered to an electric load. Recent theoretical and experimental studies on the performance of such devices are available in the literature (Sherrit et al., 2006; Bao et al., 2007;

Saulnier et al., 2006; Yang et al., 2008; Xu et al., 2009). In a realistic situation, where the elastic wall is only partially covered by finite piezoelectric patches, vibration is confined within the covered area of the plate, which is defined as “energy trapping” (Wang et al., 2007; Yang and Guo, 2008; Liu et al., 2011) and is useful in device mounting, mode interactions, and so on.

The studies discussed above assume that the interface is almost perfect. However, in addition to be damaged under harsh conditions, the interface cannot be perfect because of the presence of micro-defects and diffusion impurities, which in turn have a significant impact on the device performance (Fu et al., 2010; Cao et al., 2009). Therefore, it is essential to consider

State Key Laboratory for Strength and Vibration of Mechanical Structures, Xi'an Jiaotong University, Xi'an, PR China

Received: 3 July 2014; accepted: 1 May 2015

Corresponding author:

Feng Jin, State Key Laboratory for Strength and Vibration of Mechanical Structures, Xi'an Jiaotong University, Xi'an 710049, PR China.
Email: jinfezhao@263.net

possibly imperfect interfaces when designing and applying piezoelectric transformers. Comprehensive analyses of imperfect interfaces are presented in two review articles (Wang et al., 2000; Peter, 1992). Specifically, the shear-lag model (Cheng et al., 1997; Handge, 2002), which is the simplest description (treating the interface bonding as a layer without thickness but with elasticity and interface elastic strain energy), has been widely applied to study imperfect interfaces both theoretically (Fan et al., 2006; Li and Lee, 2010; Melkumyan and Mai, 2008) and experimentally (Jin et al., 2005; Lavrentyev and Rokhlin, 1998). However, most studies have mainly focused on elastic imperfect interfaces, and only a few have been carried out to investigate the effect of imperfect viscoelastic interfaces, which are, in fact, more realistic.

To better imitate a real situation, in this study we simultaneously apply the structural damping and shear-slip models, which simulate the effects of an imperfect viscoelastic interface on the performance of a finite elastic plate partially covered by piezoelectric patches on two sides. Using the equations of linear elasticity and piezoelectricity (Yang, 2005) to model the plate and the transducers, respectively, we mainly discuss the effect of the imperfect viscoelastic interface on the performance of the device.

2. Structure

Consider a finite elastic plate, partially covered by piezoelectric patches on two sides, such as that shown in Figure 1. The two piezoelectric patches are made of polarized ceramics with the z axis being the poling direction P or the six-fold axis (the z axis is determined by the right-hand rule from the x and y axes in the figure).

The plate has thickness $2h$, length $2L$ and is unbounded in the z direction (only a cross-section is shown). We consider it as a unit-thickness plate in the z direction. It can be made either from a metal or from a dielectric. If the plate is metallic, a very thin insulating layer is assumed to be present between the transducer electrodes and the plate. This insulating layer and the bonding interface are treated—as a whole—as the imperfect interface, as shown in Figure 1. Consider the thickness field excitation because it's easier to excite the thickness mode when the thickness of the piezoelectric patch is much smaller than its length. (where $v_1 = V_1 \exp(i\omega t)$ is a known time-harmonic driving voltage, v_2 is an unknown output voltage, I_1 and I_2 are the output currents, and Z is the impedance of the output circuit in the time-harmonic motions).

3. Governing equations

For the material orientation and electrode configuration in Figure 1, the plate can be excited to the so-called thickness-twist, anti-plane, or shear horizontal (SH) mode (Yang, 2005; Yang, 2010) with:

$$u_x = u_y = 0, \quad u_z = u(x, y, t) \tag{1}$$

3.1. Equations for the elastic plate

Consider a plate of an isotropic elastic material, the nonzero shear stress components T_{yz} and T_{zx} are:

$$T_{yz} = \mu \frac{\partial u}{\partial y}, \quad T_{zx} = \mu \frac{\partial u}{\partial x} \tag{2}$$

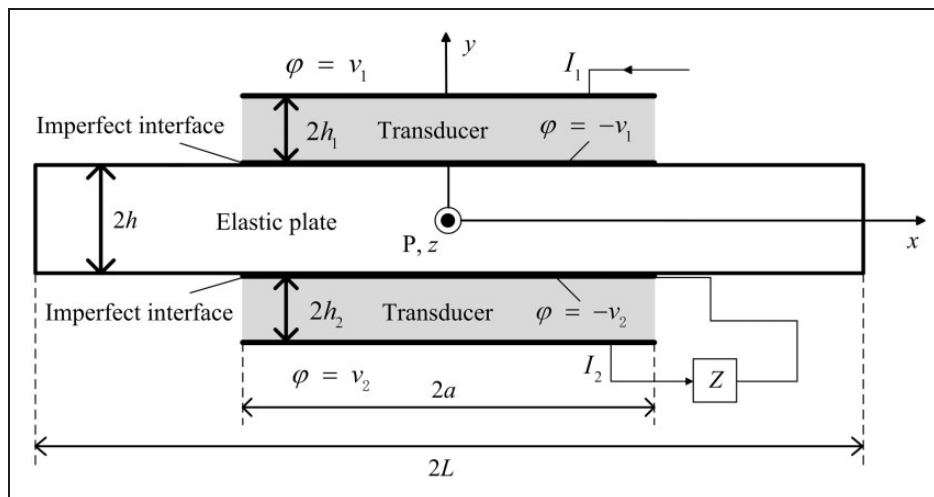


Figure 1. A finite elastic wall with two piezoelectric transducers.

where μ is the shear elastic constant. The governing equation can then be described as:

$$\nabla^2 u = -\xi^2 u \quad (3)$$

where $\nabla^2 = \partial^2 x + \partial^2 y$ is the two-dimensional Laplacian, $\xi = \frac{\omega}{\sqrt{\mu/\rho}}$, and ρ is the mass density.

3.2. Equations for the transducers

For ceramics poled in the z direction, the displacement components and electrical potential function are:

$$u_x = u_y = 0, \quad u_z = u(x, y, t), \quad \varphi = \varphi(x, y, t) \quad (4)$$

The nonzero stress and electric-displacement components are given by:

$$\begin{cases} T_{zx} \\ T_{yz} \end{cases} = c \nabla u + e \nabla \varphi, \quad \begin{cases} D_x \\ D_y \end{cases} = e \nabla u - \varepsilon \nabla \varphi \quad (5)$$

where we have denoted $c = c_{44}$, $e = e_{15}$, and $\varepsilon = \varepsilon_{11}$ for convenience with c_{44} , e_{15} , and ε_{11} to represent the elastic-constant, piezoelectric, and dielectric-permittivity coefficients of the piezoelectric material, respectively. The governing equations can be obtained as:

$$\begin{aligned} c \nabla^2 u + e \nabla^2 \varphi &= \rho_1 \frac{\partial^2 u}{\partial t^2}, \\ e \nabla^2 u - \varepsilon \nabla^2 \varphi &= 0, \end{aligned} \quad (6)$$

where ρ_1 stands for the mass density. By introducing the auxiliary function

$$\phi = \varphi - \frac{e}{\varepsilon} u \quad (7)$$

we obtain other expressions for the nonzero components and the governing equations:

$$\begin{cases} T_{zx} \\ T_{yz} \end{cases} = \bar{c} \nabla u + e \nabla \phi, \quad \begin{cases} D_x \\ D_y \end{cases} = -\varepsilon \nabla \phi \quad (8)$$

$$\begin{aligned} \nabla^2 u &= -\xi_1^2 u, \\ \nabla^2 \phi &= 0 \end{aligned} \quad (9)$$

where the wavenumber satisfies $\xi_1 = \frac{\omega}{\sqrt{\bar{c}/\rho_1}}$, and $\bar{c} = c + \frac{e^2}{\varepsilon}$ is the effective piezoelectric stiffness.

3.3. Boundary and interface conditions

At the top and bottom surfaces, as well as at the interfaces, we have:

$$\varphi(h + 2h_1) = v_1, \quad |x| < a \quad (10a)$$

$$T_{yz}(h + 2h_1) = 0, \quad |x| < a \quad (10b)$$

$$\varphi(h^-) = -v_1, \quad |x| < a \quad (10c)$$

$$T_{yz}(h^-) = \begin{cases} T_{yz}(h^+) = K'[u(h^-) - u(h^+)], & |x| < a \\ 0, & a < |x| < L \end{cases} \quad (10d)$$

$$\varphi(-h^+) = -v_2, \quad |x| < a \quad (10e)$$

$$T_{yz}(-h^-) = \begin{cases} T_{yz}(-h^+) = K''[u(-h^-) - u(-h^+)], & |x| < a \\ 0, & a < |x| < L \end{cases} \quad (10f)$$

$$\varphi(-h - 2h_2) = v_2, \quad |x| < a \quad (10g)$$

$$T_{yz}(-h - 2h_2) = 0, \quad |x| < a \quad (10h)$$

where '+' and '-' mean positive approach and negative approach along y coordinate respectively.

We apply the shear-slip model to calculate the influence of imperfect viscoelastic interfaces, thereby introducing K' and K'' , which are interface stiffness parameters that describe how well two interfaces are bonded. For perfect interfaces with a continuous displacement across the joints, $K' = \infty$ or $K'' = \infty$, whereas $K' = 0$ or $K'' = 0$ corresponds to the conditions at which no elastic interactions are present at the interface. In addition, there are traction-free boundary conditions at the edges of the plate ($x = \pm L$) and the transducers ($x = \pm a$). In the case of the transducers, the edges have no electrodes and are therefore uncharged.

4. Theoretical analysis

The input voltage is known as time-harmonic. We use the complex notation. All the fields contain an $\exp(i\omega t)$ factor, which will be dropped in the following analysis for convenience.

4.1. The elastic plate

Based on the edge conditions at $x = \pm L$, we assume the following symmetric field from the separation of the variables:

$$u = U(y) \cos \frac{n\pi x}{L}, \quad n = 0, 1, 2, \dots \quad (11)$$

Substituting equation (11) into equation (3) yields:

$$\frac{\partial^2 u}{\partial y^2} + \eta_n^2 u = 0 \quad (12)$$

where $\eta_n = \left[\xi^2 - \left(\frac{n\pi}{L} \right)^2 \right]^{1/2}$.

Then, the general solution for the u symmetric field in the x direction can be written as:

$$u = A_0 \sin(\eta_0 y) + B_0 \cos(\eta_0 y) + \sum_{n=1}^{\infty} [A_n \sin(\eta_n y) + B_n \cos(\eta_n y)] \cos \frac{n\pi x}{L} \quad (13)$$

where A_n and B_n are undetermined constants. From equation (2), we obtain:

$$T_{yz} = \mu \left\{ \eta_0 [A_0 \cos(\eta_0 y) - B_0 \sin(\eta_0 y)] + \sum_{n=1}^{\infty} \eta_n [A_n \cos(\eta_n y) - B_n \sin(\eta_n y)] \cos \frac{n\pi x}{L} \right\} \quad (14)$$

4.2. The upper transducer

Consider the following symmetric modes:

$$u = U(y) \cos \frac{m\pi x}{a}, \quad \phi = \Psi(y) \cos \frac{m\pi x}{a} \quad m = 0, 1, 2, \dots \quad (15)$$

which already satisfy the edge conditions $T_{xz} = 0$ and $D_x = 0$ at $x = \pm a$. Substitution of equation (15) into equation (9) results in:

$$\frac{\partial^2 u}{\partial y^2} + \delta_m^2 u = 0, \quad \frac{\partial^2 \phi}{\partial y^2} - \left(\frac{m\pi}{a} \right)^2 \phi = 0 \quad (16)$$

where $\delta_m = \left[\xi_1^2 - \left(\frac{m\pi}{a} \right)^2 \right]^{1/2}$.

The general solution for the u symmetric field in the x direction is:

$$u = C_0 \sin(\delta_0 y) + D_0 \cos(\delta_0 y) + \sum_{m=1}^{\infty} [C_m \sin(\delta_m y) + D_m \cos(\delta_m y)] \cos \frac{m\pi x}{a},$$

$$\phi = G_0 y + H_0 + \sum_{m=1}^{\infty} \left[G_m \sinh \frac{m\pi y}{a} + H_m \cosh \frac{m\pi y}{a} \right] \times \cos \frac{m\pi x}{a}, \quad (17)$$

where C_m , D_m , G_m and H_m are undetermined constants. The electric potential, the stress and the electric displacement can be obtained by using equations (7) and (8):

$$\varphi = \phi + \frac{e}{\varepsilon} u = G_0 y + H_0 + \frac{e}{\varepsilon} [C_0 \sin(\delta_0 y) + D_0 \cos(\delta_0 y)]$$

$$+ \sum_{m=1}^{\infty} \left\{ G_m \sinh \frac{m\pi y}{a} + H_m \cosh \frac{m\pi y}{a} + \frac{e}{\varepsilon} [C_m \sin(\delta_m y) + D_m \cos(\delta_m y)] \right\} \cos \frac{m\pi x}{a},$$

$$T_{yz} = \bar{c} u_{,y} + e \phi_{,y} = \bar{c} \delta_0 [C_0 \cos(\delta_0 y) - D_0 \sin(\delta_0 y)] + e G_0 + \sum_{m=1}^{\infty} \left\{ \bar{c} \delta_m [C_m \cos(\delta_m y) - D_m \sin(\delta_m y)] + e \frac{m\pi}{a} \left[G_m \cosh \frac{m\pi y}{a} + H_m \sinh \frac{m\pi y}{a} \right] \right\} \cos \frac{m\pi x}{a},$$

$$D_y = -\varepsilon \phi_{,y} = -\varepsilon G_0 - \sum_{m=1}^{\infty} \varepsilon \frac{m\pi}{a} \times \left[G_m \cosh \frac{m\pi y}{a} + H_m \sinh \frac{m\pi y}{a} \right] \cos \frac{m\pi x}{a} \quad (18)$$

4.3. The lower transducer

Similar to equation (17), for the lower transducer we have:

$$u = E_0 \sin(\delta_0 y) + F_0 \cos(\delta_0 y) + \sum_{m=1}^{\infty} [E_m \sin(\delta_m y) + F_m \cos(\delta_m y)] \cos \frac{m\pi x}{a},$$

$$\phi = N_0 y + R_0 + \sum_{m=1}^{\infty} \left[N_m \sinh \frac{m\pi y}{a} + R_m \cosh \frac{m\pi y}{a} \right] \times \cos \frac{m\pi x}{a} \quad (19)$$

where C_m , D_m , G_m and H_m are undetermined constants. Similarly, the corresponding electric potential, stress and electric displacement, which are needed for the boundary conditions, are given by:

$$\varphi = \phi + \frac{e}{\varepsilon} u = N_0 y + R_0 + \frac{e}{\varepsilon} [E_0 \sin(\delta_0 y) + F_0 \cos(\delta_0 y)] + \sum_{m=1}^{\infty} \left\{ N_m \sinh \frac{m\pi y}{a} + R_m \cosh \frac{m\pi y}{a} + \frac{e}{\varepsilon} [E_m \sin(\delta_m y) + F_m \cos(\delta_m y)] \right\} \cos \frac{m\pi x}{a},$$

$$T_{yz} = \bar{c} \delta_0 [E_0 \cos(\delta_0 y) - F_0 \sin(\delta_0 y)] + e N_0 + \sum_{m=1}^{\infty} \left\{ \bar{c} \delta_m [E_m \cos(\delta_m y) - F_m \sin(\delta_m y)] + e \frac{m\pi}{a} \left[N_m \cosh \frac{m\pi y}{a} + R_m \sinh \frac{m\pi y}{a} \right] \right\} \cos \frac{m\pi x}{a},$$

$$D_{12} = -\varepsilon N_0 - \sum_{m=1}^{\infty} \varepsilon \frac{m\pi}{a} \left[N_m \cosh \frac{m\pi y}{a} + R_m \sinh \frac{m\pi y}{a} \right] \times \cos \frac{m\pi x}{a} \quad (20)$$

4.4. Boundary, interface, and circuit conditions

By substituting equations (13), (14), (17), (18), (19), and (20) into the boundary and interface conditions given in equation (10), we obtain:

$$\begin{aligned}
 &G_0(h + 2h_1) + H_0 + \frac{e}{\varepsilon}[C_0 \sin \delta_0(h + 2h_1) \\
 &+ D_0 \cos \delta_0(h + 2h_1)] \\
 &+ \sum_{m=1}^{\infty} \left\{ G_m \sinh \frac{m\pi(h + 2h_1)}{a} + H_m \cosh \frac{m\pi(h + 2h_1)}{a} \right. \\
 &+ \left. \frac{e}{\varepsilon}[C_m \sin \delta_m(h + 2h_1) + D_m \cos \delta_m(h + 2h_1)] \right\} \\
 &\times \cos\left(\frac{m\pi x}{a}\right) = V_1, \quad |x| < a \tag{21a}
 \end{aligned}$$

$$\begin{aligned}
 &\bar{c}\delta_0[C_0 \cos \delta_0(h + 2h_1) - D_0 \sin \delta_0(h + 2h_1)] + eG_0 \\
 &+ \sum_m^{\infty} \left\{ \bar{c}\delta_m[C_m \cos \delta_m(h + 2h_1) - D_m \sin \delta_m(h + 2h_1)] \right. \\
 &+ \left. e \frac{m\pi}{a} \left[G_m \cosh \frac{m\pi(h + 2h_1)}{a} + H_m \sinh \frac{m\pi(h + 2h_1)}{a} \right] \right\} \\
 &\times \cos\left(\frac{m\pi x}{a}\right) = 0, \quad |x| < a \tag{21b}
 \end{aligned}$$

$$\begin{aligned}
 &G_0h + H_0 + \frac{e}{\varepsilon}[C_0 \sin(\delta_0h) + D_0 \cos(\delta_0h)] \\
 &+ \sum_{m=1}^{\infty} \left\{ G_m \sinh \frac{m\pi h}{a} + H_m \cosh \frac{m\pi h}{a} \right. \\
 &+ \left. \frac{e}{\varepsilon}[C_m \sin(\delta_mh) + D_m \cos(\delta_mh)] \right\} \cos\left(\frac{m\pi x}{a}\right) \\
 &= -V_1, \quad |x| < a \tag{21c}
 \end{aligned}$$

$$\begin{aligned}
 &\mu\eta_0[A_0 \cos(\eta_0h) - B_0 \sin(\eta_0h)] \\
 &+ \sum_{n=1}^{\infty} \left\{ \mu\eta_n[A_n \cos(\eta_nh) - B_n \sin(\eta_nh)] \right\} \cos \frac{n\pi x}{L} \\
 &= \begin{cases} \bar{c}\delta_0[C_0 \cos(\delta_0h) - D_0 \sin(\delta_0h)] + eG_0 \\ \quad + \sum_{m=1}^{\infty} \left\{ \bar{c}\delta_m[C_m \cos(\delta_mh) \right. \\ \quad \left. - D_m \sin(\delta_mh)] + e \frac{m\pi}{a} \right. \\ \quad \left. \times \left[G_m \cosh \frac{m\pi h}{a} + H_m \sinh \frac{m\pi h}{a} \right] \right\} \\ \quad \cos\left(\frac{m\pi x}{a}\right), & |x| < a \\ 0, & a < |x| < L \end{cases} \tag{21d}
 \end{aligned}$$

$$\begin{aligned}
 &\mu\eta_0[A_0 \cos(\eta_0h) - B_0 \sin(\eta_0h)] \\
 &+ \sum_{n=1}^{\infty} \left\{ \mu\eta_n[A_n \cos(\eta_nh) - B_n \sin(\eta_nh)] \right\} \cos \frac{n\pi x}{L}
 \end{aligned}$$

$$\begin{aligned}
 &= K' \left\{ C_0 \sin(\delta_0h) + D_0 \cos(\delta_0h) - A_0 \sin(\eta_0h) - B_0 \cos(\eta_0h) \right. \\
 &+ \sum_{m=1}^{\infty} [C_m \sin(\delta_mh) + D_m \cos(\delta_mh)] \cos\left(\frac{m\pi x}{a}\right) \\
 &- \left. \sum_{n=1}^{\infty} [A_n \sin(\eta_nh) + B_n \cos(\eta_nh)] \cos\left(\frac{n\pi x}{L}\right) \right\}, \quad |x| < a \\
 &- N_0h + R_0 - \frac{e}{\varepsilon}[E_0 \sin(\delta_0h) - F_0 \cos(\delta_0h)] \\
 &+ \sum_{m=1}^{\infty} \left\{ -N_m \sinh \frac{m\pi h}{a} + R_m \cosh \frac{m\pi h}{a} \right. \\
 &- \left. \frac{e}{\varepsilon}[E_m \sin(\delta_mh) - F_m \cos(\delta_mh)] \right\} \\
 &\times \cos\left(\frac{m\pi x}{a}\right) = -V_2, \quad |x| < a \tag{21f}
 \end{aligned}$$

$$\begin{aligned}
 &\mu\eta_0[A_0 \cos(\eta_0h) + B_0 \sin(\eta_0h)] \\
 &+ \sum_{n=1}^{\infty} \left\{ \mu\eta_n[A_n \cos(\eta_nh) + B_n \sin(\eta_nh)] \right\} \cos \frac{n\pi x}{L} \\
 &= \begin{cases} \bar{c}\delta_0[E_0 \cos(\delta_0h) + F_0 \sin(\delta_0h)] + eN_0 \\ \quad + \sum_{m=1}^{\infty} \left\{ \bar{c}\delta_m[E_m \cos(\delta_mh) \right. \\ \quad \left. + F_m \sin(\delta_mh)] \right. \\ \quad \left. + e \frac{m\pi}{a} \left[N_m \cosh \frac{m\pi h}{a} \right. \right. \\ \quad \left. \left. - R_m \sinh \frac{m\pi h}{a} \right] \right\} \\ \quad \times \cos\left(\frac{m\pi x}{a}\right), & |x| < a \\ 0, & a < |x| < L \end{cases} \tag{21g}
 \end{aligned}$$

$$\begin{aligned}
 &\mu\eta_0[A_0 \cos(\eta_0h) + B_0 \sin(\eta_0h)] \\
 &+ \sum_{n=1}^{\infty} \left\{ \mu\eta_n[A_n \cos(\eta_nh) + B_n \sin(\eta_nh)] \right\} \cos \frac{n\pi x}{L} \\
 &= K'' \left\{ -A_0 \sin(\eta_0h) + B_0 \cos(\eta_0h) \right. \\
 &+ E_0 \sin(\delta_0h) - F_0 \cos(\delta_0h) \\
 &+ \sum_{n=1}^{\infty} [-A_n \sin(\eta_nh) + B_n \cos(\eta_nh)] \cos\left(\frac{n\pi x}{L}\right) \\
 &+ \sum_{m=1}^{\infty} [E_m \sin(\delta_mh) - F_m \cos(\delta_mh)] \\
 &\times \cos\left(\frac{m\pi x}{a}\right) \left. \right\}, \quad |x| < a \tag{21h}
 \end{aligned}$$

$$\begin{aligned}
& N_0(-h - 2h_2) + R_0 \\
& + \frac{e}{\varepsilon} [E_0 \sin \delta_0(-h - 2h_2) + F_0 \cos \delta_0(-h - 2h_2)] \\
& + \sum_{m=1}^{\infty} \left\{ N_m \sinh \frac{m\pi(-h - 2h_2)}{a} + R_m \cosh \frac{m\pi(-h - 2h_2)}{a} \right. \\
& \left. + \frac{e}{\varepsilon} [E_m \sin \delta_m(-h - 2h_2) + F_m \cos \delta_m(-h - 2h_2)] \right\} \\
& \times \cos\left(\frac{m\pi x}{a}\right) = V_2, \quad |x| < a \\
& \bar{c}\delta_0[E_0 \cos \delta_0(-h - 2h_2) - F_0 \sin \delta_0(-h - 2h_2)] + eN_0 \\
& + \sum_{m=1}^{\infty} \left\{ \bar{c}\delta_m[E_m \cos \delta_m(-h - 2h_2) - F_m \sin \delta_m(-h - 2h_2)] \right. \\
& \left. + e \frac{m\pi}{a} \left[N_m \cosh \frac{m\pi(-h - 2h_2)}{a} \right. \right. \\
& \left. \left. + R_m \sinh \frac{m\pi(-h - 2h_2)}{a} \right] \right\} \cos\left(\frac{m\pi x}{a}\right) = 0, \quad |x| < a
\end{aligned} \tag{21j}$$

Equations (21d) and (21g) are multiplied by $\cos \frac{p\pi x}{L}$ and then integrated (from $-L$ to L) for $p=0, 1, 2, 3, \dots$, and the other equations (21) are multiplied by $\cos \frac{p\pi x}{a}$ and then integrated (from $-a$ to a) for $p=0, 1, 2, 3, \dots$ to obtain the linear algebraic equations for the undetermined coefficients as follows:

If $p=0$, the linear algebraic equations for the undetermined coefficients are:

$$\begin{aligned}
& \frac{e}{\varepsilon} [C_0 \sin \delta_0(h + 2h_1) + D_0 \cos \delta_0(h + 2h_1)] \\
& + G_0(h + 2h_1) + H_0 = V_1
\end{aligned} \tag{22a}$$

$$\bar{c}\delta_0[C_0 \cos \delta_0(h + 2h_1) - D_0 \sin \delta_0(h + 2h_1)] + eG_0 = 0 \tag{22b}$$

$$\frac{e}{\varepsilon} [C_0 \sin(\delta_0 h) + D_0 \cos(\delta_0 h)] + G_0 h + H_0 = -V_1 \tag{22c}$$

$$\begin{aligned}
& \mu\eta_0[A_0 \cos(\eta_0 h) - B_0 \sin(\eta_0 h)]2L \\
& = \{\bar{c}\delta_0[C_0 \cos(\delta_0 h) - D_0 \sin(\delta_0 h)] + eG_0\}2a
\end{aligned} \tag{22d}$$

$$\begin{aligned}
& \left[-\frac{\mu}{K'} \eta_0 \cos(\eta_0 h) + \sin(\eta_0 h) \right] A_0 \\
& + \left[\frac{\mu}{K'} \eta_0 \sin(\eta_0 h) + \cos(\eta_0 h) \right] B_0 \\
& - \sin(\delta_0 h) C_0 - \cos(\delta_0 h) D_0 \\
& + \frac{1}{2a} \sum_{n=1}^{\infty} \left\{ \left[-\frac{\mu}{K'} \eta_n \cos(\eta_n h) + \sin(\eta_n h) \right] A_n \right. \\
& \left. + \left[\frac{\mu}{K'} \eta_n \sin(\eta_n h) + \cos(\eta_n h) \right] B_n \right\} \int_{-a}^a \cos \frac{n\pi x}{L} dx = 0,
\end{aligned} \tag{22e}$$

$$-\frac{e}{\varepsilon} [E_0 \sin(\delta_0 h) - F_0 \cos(\delta_0 h)] - N_0 h + R_0 = -V_2 \tag{22f}$$

$$\begin{aligned}
& \mu\eta_0[A_0 \cos(\eta_0 h) + B_0 \sin(\eta_0 h)]2L \\
& = \{\bar{c}\delta_0[E_0 \cos(\delta_0 h) + F_0 \sin(\delta_0 h)] + eN_0\}2a
\end{aligned} \tag{22g}$$

$$\begin{aligned}
& \left[-\frac{\mu}{K'} \eta_0 \cos(\eta_0 h) + \sin(\eta_0 h) \right] A_0 \\
& - \left[\frac{\mu}{K'} \eta_0 \sin(\eta_0 h) + \cos(\eta_0 h) \right] B_0 \\
& - \sin(\delta_0 h) E_0 + \cos(\delta_0 h) F_0 \\
& + \frac{1}{2a} \sum_{n=1}^{\infty} \left\{ \left[-\frac{\mu}{K'} \eta_n \cos(\eta_n h) + \sin(\eta_n h) \right] A_n \right. \\
& \left. - \left[\frac{\mu}{K'} \eta_n \sin(\eta_n h) + \cos(\eta_n h) \right] B_n \right\} \int_{-a}^a \cos \frac{n\pi x}{L} dx = 0
\end{aligned} \tag{22h}$$

$$\begin{aligned}
& -\frac{e}{\varepsilon} [E_0 \sin \delta_0(h + 2h_2) - F_0 \cos \delta_0(h + 2h_2)] \\
& - N_0(h + 2h_2) + R_0 = V_2
\end{aligned} \tag{22i}$$

$$\bar{c}\delta_0[E_0 \cos \delta_0(h + 2h_2) + F_0 \sin \delta_0(h + 2h_2)] + eN_0 = 0 \tag{22j}$$

If $p > 0$, the linear algebraic equations for the undetermined coefficients can be written as:

$$\begin{aligned}
& \frac{e}{\varepsilon} [C_p \sin \delta_p(h + 2h_1) + D_p \cos \delta_p(h + 2h_1)] \\
& + G_p \sinh \frac{p\pi(h + 2h_1)}{a} + H_p \cosh \frac{p\pi(h + 2h_1)}{a} = 0
\end{aligned} \tag{23a}$$

$$\begin{aligned}
& \bar{c}\delta_p [C_p \cos \delta_p(h + 2h_1) - D_p \sin \delta_p(h + 2h_1)] \\
& + e \frac{p\pi}{a} \left[G_p \cosh \frac{p\pi(h + 2h_1)}{a} \right. \\
& \left. + H_p \sinh \frac{p\pi(h + 2h_1)}{a} \right] = 0,
\end{aligned} \tag{23b}$$

$$\begin{aligned}
& \frac{e}{\varepsilon} [C_p \sin(\delta_p h) + D_p \cos(\delta_p h)] + G_p \sinh \frac{p\pi h}{a} \\
& + H_p \cosh \frac{p\pi h}{a} = 0
\end{aligned} \tag{23c}$$

$$\begin{aligned}
& \mu\eta_p [A_p \cos(\eta_p h) - B_p \sin(\eta_p h)] \\
& L = \{\bar{c}\delta_0[C_0 \cos(\delta_0 h) - D_0 \sin(\delta_0 h)] + eG_0\} \\
& \times \int_{-a}^a \cos \frac{p\pi x}{L} dx + \sum_{m=1}^{\infty} \left\{ \bar{c}\delta_m \left[\begin{array}{l} C_m \cos(\delta_m h) \\ - D_m \sin(\delta_m h) \end{array} \right] \right. \\
& \left. \times \left\{ +e \frac{m\pi}{a} \left[G_m \cosh \frac{m\pi h}{a} + H_m \sinh \frac{m\pi h}{a} \right] \right\} W_{mp}, \right.
\end{aligned} \tag{23d}$$

$$\sum_{n=1}^{\infty} \left\{ \left[-\frac{\mu}{K'} \eta_n \cos(\eta_n h) + \sin(\eta_n h) \right] A_n + \left[\frac{\mu}{K'} \eta_n \sin(\eta_n h) + \cos(\eta_n h) \right] B_n \right\} W_{np} - [C_p \sin(\delta_p h) + D_p \cos(\delta_p h)] a = 0, \quad (23e)$$

$$-\frac{e}{\varepsilon} [E_p \sin(\delta_p h) - F_p \cos(\delta_p h)] - N_p \sinh \frac{p\pi h}{a} + R_p \cosh \frac{p\pi h}{a} = 0 \quad (23f)$$

$$\begin{aligned} & \mu \eta_p [A_p \cos(\eta_p h) + B_p \sin(\eta_p h)] \\ L = & \left\{ \bar{c} \delta_0 [E_0 \cos(\delta_0 h) + F_0 \sin(\delta_0 h)] + e N_0 \right\} \\ & \times \int_{-a}^a \cos \frac{p\pi x}{L} dx \\ & + \sum_{m=1}^{\infty} \left\{ \bar{c} \delta_m [E_m \cos(\delta_m h) + F_m \sin(\delta_m h)] \right. \\ & \left. + e \frac{m\pi}{a} \left[N_m \cosh \frac{m\pi h}{a} - R_m \sinh \frac{m\pi h}{a} \right] \right\} W_{mp} \end{aligned} \quad (23g)$$

$$\begin{aligned} & \sum_{n=1}^{\infty} \left\{ \left[-\frac{\mu}{K'} \eta_n \cos(\eta_n h) + \sin(\eta_n h) \right] \right. \\ & \times A_n - \left[\frac{\mu}{K'} \eta_n \sin(\eta_n h) + \cos(\eta_n h) \right] B_n \left. \right\} W_{np} \\ & - [E_p \sin(\delta_p h) - F_p \cos(\delta_p h)] a = 0, \\ & -\frac{e}{\varepsilon} [E_p \sin \delta_p (h + 2h_2) - F_p \cos \delta_p (h + 2h_2)] \\ & - N_p \sinh \frac{p\pi (h + 2h_2)}{a} + R_p \cosh \frac{p\pi (h + 2h_2)}{a} = 0 \end{aligned} \quad (23i)$$

$$\begin{aligned} & \bar{c} \delta_p [E_p \cos \delta_p (h + 2h_2) + F_p \sin \delta_p (h + 2h_2)] \\ & + e \frac{p\pi}{a} \left[N_p \cosh \frac{p\pi (h + 2h_2)}{a} - R_p \sinh \frac{p\pi (h + 2h_2)}{a} \right] = 0 \end{aligned} \quad (23j)$$

where $W_{mp} = \int_{-a}^a \cos \frac{m\pi x}{a} \cos \frac{p\pi x}{L} dx$, $W_{np} = \int_{-a}^a \cos \frac{n\pi x}{L} \cos \frac{p\pi x}{a} dx$. When $K' = K'' = \infty$, Equations (22) and (23) have exactly the same expression as that obtained by Yang et al. (2008), which confirms the accuracy of the theoretical derivation. In addition, to calculate the charge and current on the upper electrode of the upper transducer, we have:

$$\begin{aligned} Q_1 &= \int_{-a}^a -D_y|_{y=h+2h_1} dx, \\ I_1 &= \dot{Q}_1 = i\omega Q_1 \end{aligned} \quad (24)$$

Similarly, for the charge and current on the lower electrode of the lower transducer, we obtain:

$$\begin{aligned} Q_2 &= \int_{-a}^a D_y|_{y=-h-2h_2} dx, \\ I_2 &= -\dot{Q}_2 = -i\omega Q_2 \end{aligned} \quad (25)$$

For the output-circuit conditions of the time-harmonic motions, we have:

$$I_2 = 2V_2/Z \quad (26)$$

and substituting equations (25) and (20) into equation (26) results in:

$$\begin{aligned} -i\omega \int_{-a}^a \left\{ -\varepsilon N_0 - \sum_{m=1}^{\infty} \varepsilon \frac{m\pi}{a} \left[N_m \cosh \frac{m\pi(-h-2h_2)}{a} \right. \right. \\ \left. \left. + R_m \sinh \frac{m\pi(-h-2h_2)}{a} \right] \cos \left(\frac{m\pi x}{a} \right) \right\} dx = \frac{2V_2}{Z} \end{aligned} \quad (27)$$

The input and output powers are given by equation (28)

$$\begin{aligned} P_1 &= \frac{1}{4} (I_1 \cdot 2V_1^* + I_1^* \cdot 2V_1), \\ P_2 &= \frac{1}{4} (I_2 \cdot 2V_2^* + I_2^* \cdot 2V_2) \end{aligned} \quad (28)$$

where an asterisk denotes a complex conjugate. The efficiency of the system can then be written as:

$$\lambda = P_2/P_1 \quad (29)$$

5. Numerical results and discussion

An elastic layer made of steel (with $\mu = 2.69 \times 10^{11}$ N/m² and $\rho = 7850$ kg/m³) is used as an example for the numerical simulations. We assume that the upper and lower transducers are both made from the piezoelectric lead-zirconium-titanate-based ceramic (PZT-5 H; with $c_{44} = 2.30 \times 10^{10}$ N/m², $e_{15} = 17$ C/m², $\varepsilon_{11} = 1.505 \times 10^{-8}$ F/m, and $\rho_1 = 7500$ kg/m³ (Auld, 1973)). As geometric parameters, we choose $a = 0.05$ m, $L = 3a$, $h = a/10$, and $h_2 = h_1$. $Z_0 = \frac{1}{i\omega C_0}$ ($C_0 = \frac{\varepsilon_{11} a}{h_1}$) is introduced as a unit for the load. The effects of Z on piezoelectric transformers performances are discussed by Hu et al. (2003) and Yang et al. (2008), here, we fix $Z = iZ_0$ for convenience. We also fix $V_1 = 220$ V and introduce the fundamental thickness-shear frequency of the plate

$\omega_0 = \frac{\pi}{2h} \sqrt{\frac{\mu}{\rho}} = 1.839 \times 10^6$ rad/s in the following simulations for convenience. The structural damping effect, which exists in all systems, is introduced by assuming that the elastic-material constant is complex (Holland and EerNisse, 1968), that is, by replacing μ and c_{44} by $\mu(1 + iQ^{-1})$ and $c_{44}(1 + iQ^{-1})$, respectively. Generally, different materials have different Q values ranging from 10^2 to 10^3 (Holland and EerNisse, 1968). In our calculations, we use $Q = 10^3$ in all cases for simplicity. We also consider the two interface stiffness parameters K' and K'' as a single complex interface stiffness K , given by $K = K_1 + iK_2$, in which K_1 and K_2 are real variables, and the imaginary part describes the interface damping to imitate a viscoelastic interface. Although this is actually impossible in practice, the treatment described herein is helpful for investigating and understanding the effects of imperfect viscoelastic interfaces on the characteristics of piezoelectric transformers.

In the following discussion, we mainly focus on the effect of an imperfect interface on the system based on the energy-trapping phenomenon (Wang et al., 2007; Yang and Guo, 2008; Liu et al., 2011). Hence, the input frequency meets: $\omega_0(1 - R_0) < \omega < \omega_0$ (Kong et al., 2011), where $R_0 = \frac{\rho_1(h_1 + h_2)}{\rho h}$.

5.1. Convergence and verification of the series

Firstly, we examine the convergence and verification of the series for a perfect interface. Table 1 shows the first resonance frequencies, transformation ratios, and efficiencies for selected thickness ratios h_1/h upon varying the expansion term of the series. While the performance of the transducer can be altered by changing the thickness ratio h_1/h , the convergence of the series does not change. The transformation ratio and the efficiency increase at higher h_1/h ratios, whereas the first resonance frequency decreases as h_1/h increases. From the results shown in Table 1, we conclude that ten expansion terms are enough to ensure five significant figures in the calculation. The term $\eta_n(\delta_m)$ can be positive under such conditions, and if relatively larger n and m values are needed, η_n and δ_m can be redefined with a minus sign, and the sine and cosine functions in equations (13), (17) and (19) can be changed to hyperbolic sine and cosine functions, respectively (He et al., 2011). Therefore, all the following calculations are carried out using ten terms in the series.

5.2. The effect of an imperfect viscoelastic interface

Figure 2 shows the displacement distributions of the central plate at the first resonance for selected thickness ratios h_1/h of a perfect interface. We can see that the displacements are confined in the covered transducer

Table 1. Values of the resonance frequency, transformation ratio, and efficiency, together with the expansion terms of the series.

h_1/h ($h_2 = h_1$)	Expansion term	First resonance frequency (ω/ω_0)	Transformation ratio ($ V_2/V_1 $)	Efficiency (λ)
0.02	10	0.968367	0.150528	0.071541
	11	0.968364	0.150527	0.071545
	12	0.968369	0.150525	0.071548
0.04	10	0.932248	0.874249	0.411119
	11	0.932240	0.874245	0.411118
	12	0.932240	0.874244	0.411117
0.06	10	0.895638	1.652315	0.759494
	11	0.895636	1.652318	0.759488
	12	0.895634	1.652318	0.759486

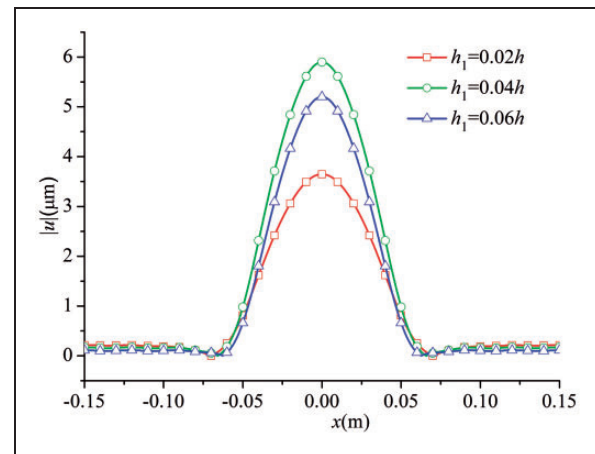


Figure 2. Displacement distributions of the central plate at the first resonance for selected thickness ratios h_1/h of a perfect interface, ($\gamma = h$, $K = \infty$).

area at the first resonance, and when $h_1 = 0.06h$, the displacement vanishes more rapidly at the two edges of the elastic plate than that of other two thickness ratios, revealing better effect of energy trapping. This is because the mass of the transducer plays a dominant role in this system. Without loss of any generality, we choose $h_1 = 0.06h$ in the following calculations, although in reality, to obtain a high performance, an appropriate thickness ratio should be considered after careful calculations.

Figures 3–5 reveal the displacement u , and the stress components T_{yz} and T_{zx} for the three trapped modes, respectively. Clearly, the displacement and stress component T_{yz} are symmetric about the y axis, which corresponds to the symmetric displacement field hypothesis described in equation (13). On the contrary,

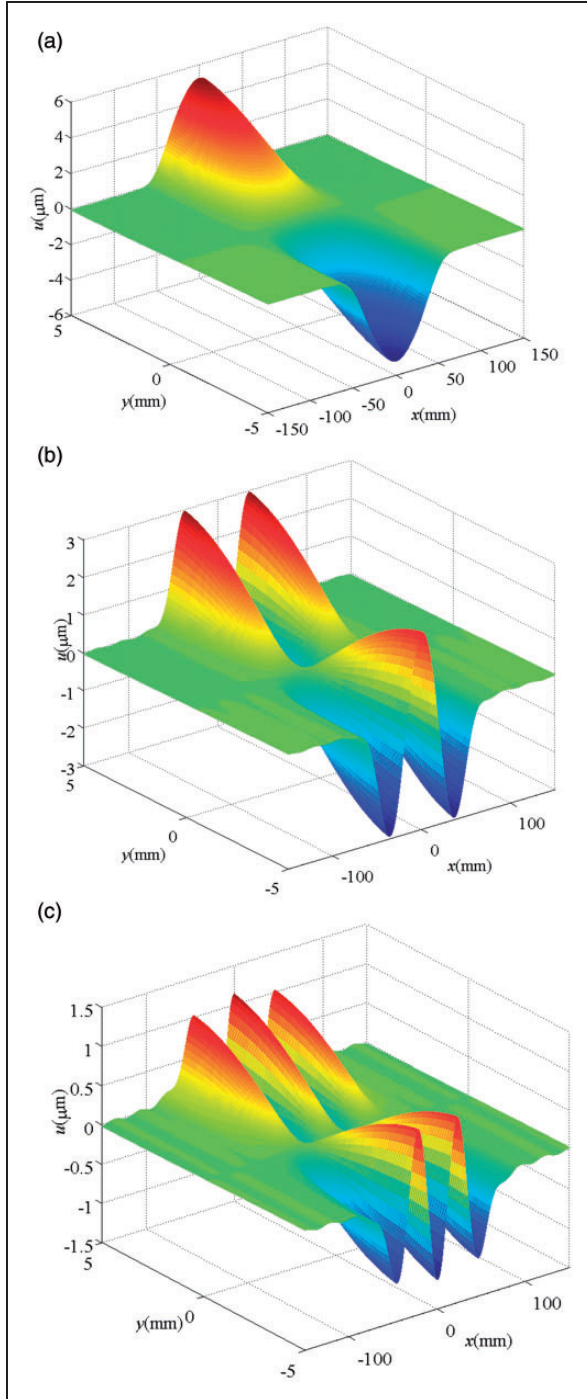


Figure 3. Displacement u of the first three trapped modes, ($h_2 = h_1 = 0.06h$, $K = \infty$): (a) first mode, $\omega = 0.89563\omega_0$; (b) second mode, $\omega = 0.91975\omega_0$ and (c) third mode, $\omega = 0.96962\omega_0$.

the stress component T_{zx} is anti-symmetric about the y axis. Because of the effects of the two transducers, the vibration is only confined in the region $|x| < a$, out of where u , T_{yz} , and T_{zx} are almost equal to zero, which is

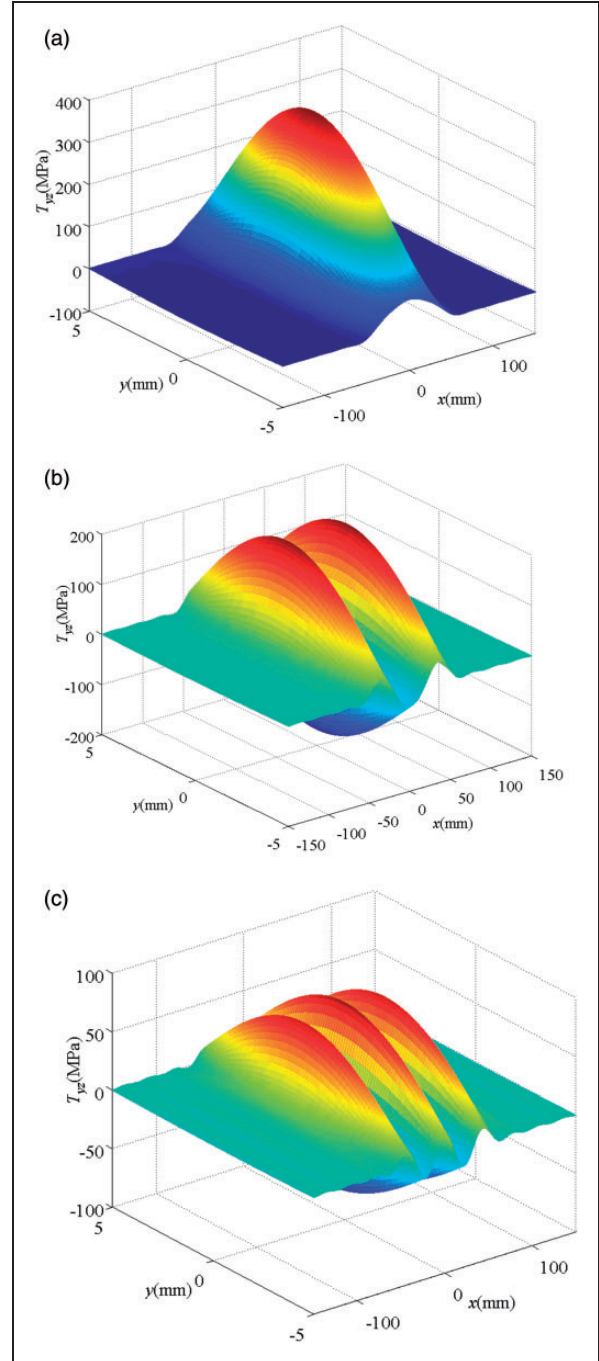


Figure 4. Stress component T_{yz} of the first three trapped modes, ($h_2 = h_1 = 0.06h$, $K = \infty$): (a) first mode, $\omega = 0.89563\omega_0$; (b) second mode, $\omega = 0.91975\omega_0$ and (c) third mode, $\omega = 0.96962\omega_0$.

related to the so-called energy-trapping phenomenon. The fact that T_{yz} is equivalent to zero in the region $a < |x| < L$ can be explained by the boundary conditions of (10d) and (10f), which can certify the validity of the numerical stimulation. When the energy-trapping

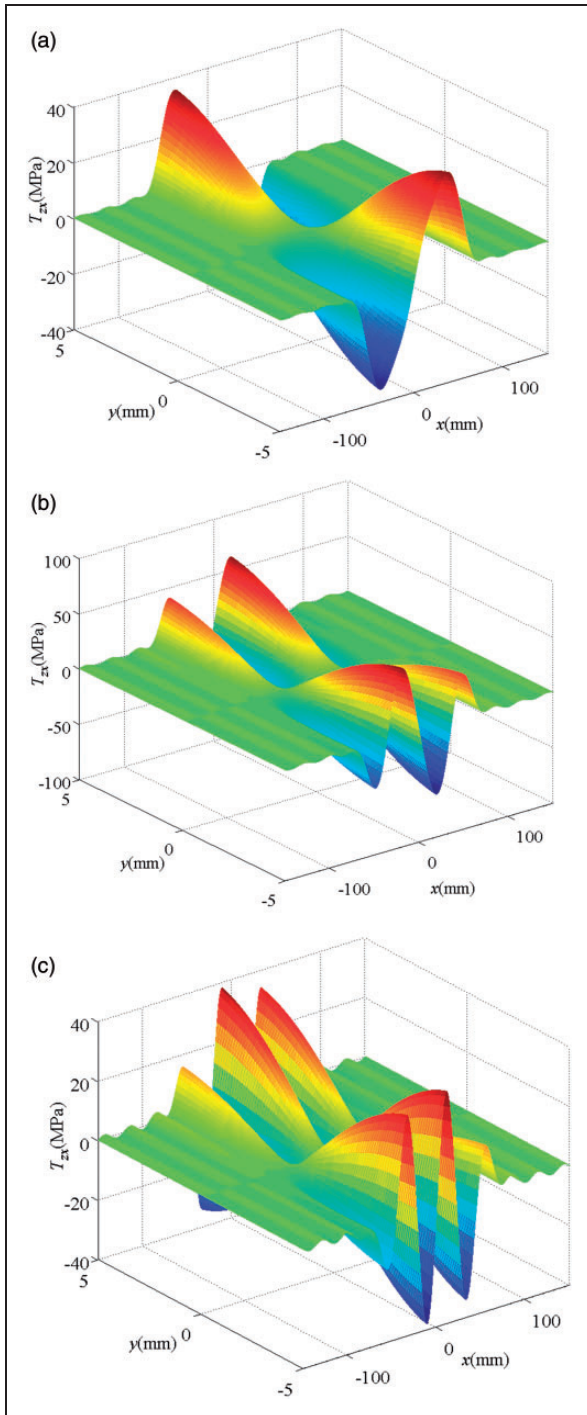


Figure 5. Stress component T_{zx} of the first three trapped modes, ($h_2 = h_1 = 0.06h$, $K = \infty$): (a) first mode, $\omega = 0.89563\omega_0$; (b) second mode, $\omega = 0.91975\omega_0$ and (c) third mode, $\omega = 0.96962\omega_0$.

is happening, as the device is mounted by the part where no vibration happens, the whole device vibration will not be affected.

Figure 6 shows the transformation ratio $|V_2/V_1|$ and the efficiency λ as a function of the driving frequency at

$h_1 = 0.06h$ for two selected interface situations (as stated before, $K = \infty$ means a perfect interface). The transformation ratio reaches its maxima at the resonant frequencies (as expected), with the highest values normally being observed at the first resonance. However, not all the highest transformation ratios are actually achieved at the first resonance, which depend on the system parameters, such as the thickness ratio h_1/h , material and interface properties. The highest transformation ratio is achieved at the fourth resonance by Hu et al. (2003) because of different system parameters. In addition, the transformation ratio at the third resonant frequency is so small that it can barely be determined, which demonstrates that this parameter decreases quickly upon increasing the resonance mode. At higher resonances, the corresponding modes have nodal points, and voltage cancellation usually occurs along the y direction in the output portion. Even though the efficiency is irregular throughout the whole range of trapping frequencies, it reaches its maximum values near the resonant frequencies, with the highest efficiencies also appearing at the first resonance. If the interface becomes weaker, the resonant frequency, the peak value of the transformation ratio, and the efficiency all decrease accordingly, which shows that an imperfect bonding interface can significantly affect the behavior of piezoelectric transducer systems.

Since the transformation ratio attains its maximum value at the first resonance, the following discussion will concentrate on the influence of the viscoelastic interface on the first mode. The impacts of the interface parameters K_1 and K_2 on the transformation ratio, efficiency, and displacement distribution at $x = h$ are revealed in Figures 7, 8 and 9, respectively. In Figure 7, set $K = (k_1 + 0.02i) \times 10^{15} \text{ N/m}^3$, that is, $K_2 = 0.02 \times 10^{15} \text{ N/m}^3$, $K_1 = k_1 \times 10^{15} \text{ N/m}^3$, and K_1 is proportional to k_1 , which means the variations and effects of k_1 are equivalent to those of K_1 . Similarly, set $K = (1 + k_2i) \times 6 \times 10^{14} \text{ N/m}^3$ in Figure 8, with the variations and effects of k_2 being equivalent to those of K_2 . The transformation ratio, efficiency, and displacement peak at $x = h$ increase upon increasing k_1 but decrease when k_1 remains constant and k_2 increases. The reason for this is that an increase in K_2 , which represents the interface damping, causes a growth in the system's damping, thereby leading to higher energy wastage. On the other hand, the effect of K_1 on the resonant frequency is prominent, whereas that of K_2 is almost negligible, as shown in Figure 8(a). In fact, the resonant frequency is not sensitive to K_2 , and the reason why changing this parameter causes a small shift in the resonant frequency is that we calculate the modulus of $|V_2/V_1|$ rather than V_2/V_1 .

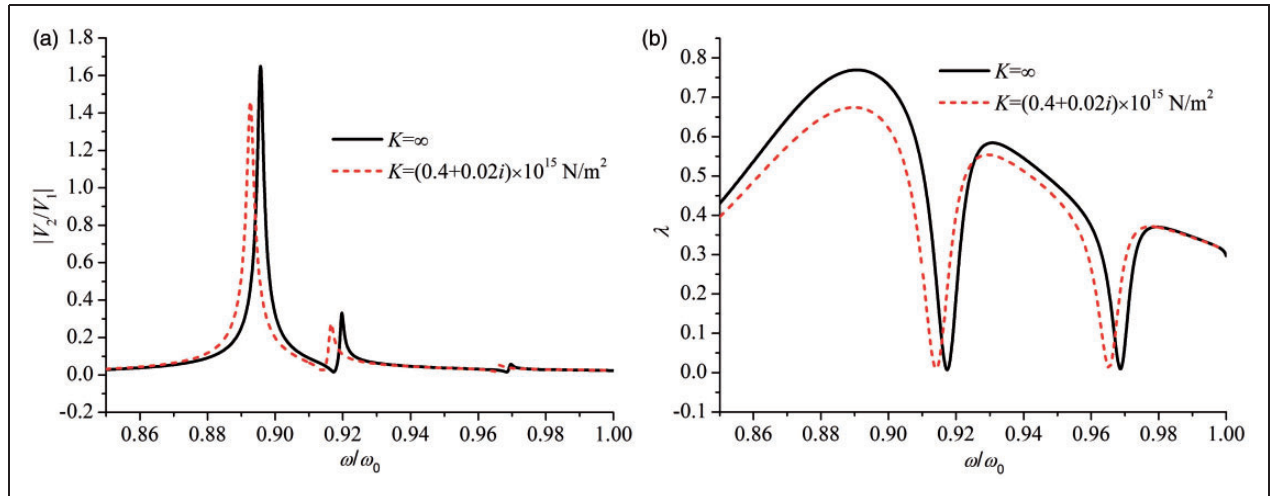


Figure 6. A few resonances of the transformation ratio $|V_2/V_1|$ and the efficiency λ versus the driving frequency, ($h_2 = h_1 = 0.06h$): (a) transformation ratio $|V_2/V_1|$ and (b) efficiency λ .

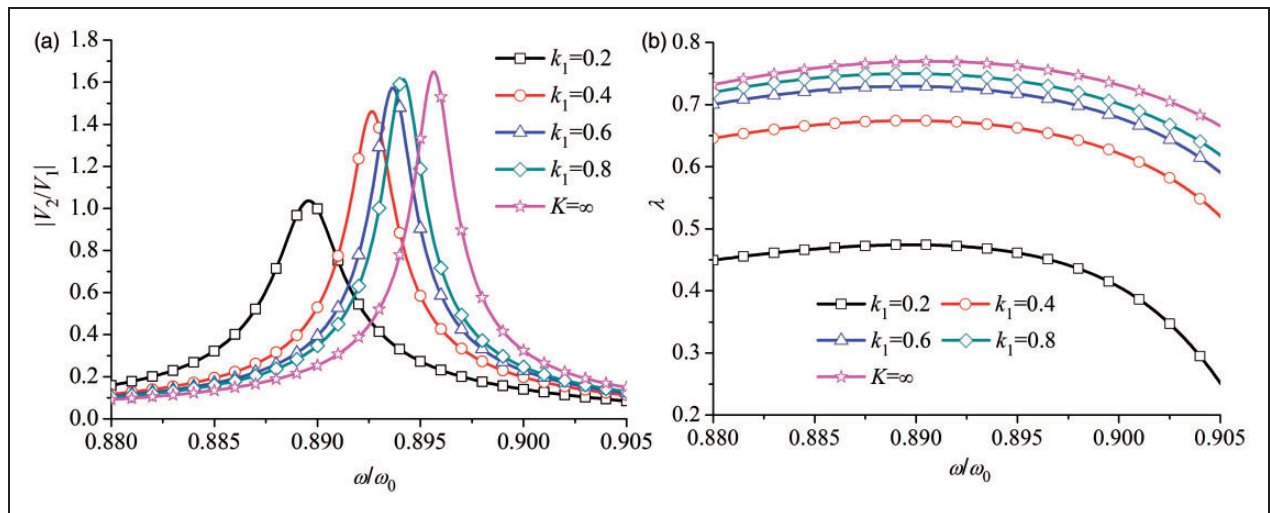


Figure 7. First resonance of the transformation ratio $|V_2/V_1|$ and the efficiency λ versus the driving frequency for selected k_1 values, ($K_1 = k_1 \times 10^{15} \text{ N/m}^3$, $K_2 = 0.02 \times 10^{15} \text{ N/m}^3$): (a) transformation ratio $|V_2/V_1|$ and (b) efficiency λ .

6. Conclusions

The shear-slip interface model is applied to study the influence of the interface parameters of a viscoelastic interface on a structure consisting of a finite elastic plate, partially covered by piezoelectric patches on two sides. We obtain a theoretical solution for the symmetric thickness–twist mode in the x direction. Numerical results confirm the good convergence and high precision of the method. If an appropriate thickness ratio h_1/h is chosen, the energy-trapping phenomenon is well presented, and the displacement and stress component T_{yz} are found to be symmetric

about the y axis (inversely, the stress component T_{zx} is anti-symmetric about this axis). The results also suggest that an imperfect bonding interface can significantly affect the behavior of piezoelectric transducer systems. If K_2 is kept constant and K_1 is increased, the amplitudes of the transformation ratio, efficiency and displacement—as well as the resonant frequency—of the system decrease. K_2 affects all the performance parameters in the opposite way, except for the resonant frequency, which is not sensitive to the interface damping parameter K_2 . These observations reveal that the amplitudes of the transformation ratio, efficiency and displacement decrease for weaker interfaces, which can provide a theoretical

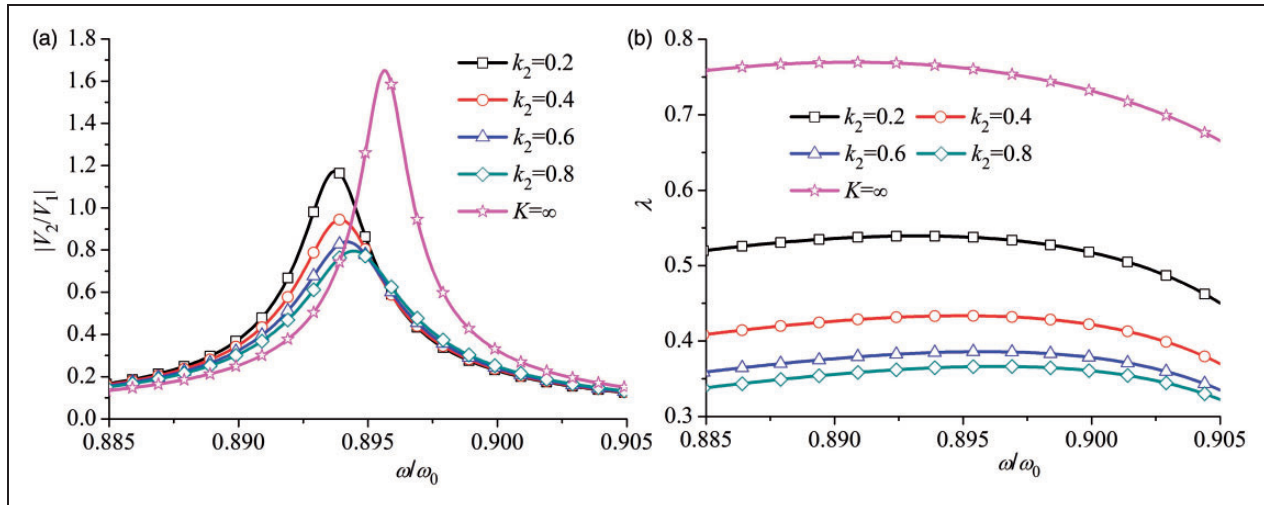


Figure 8. First resonance of the transformation ratio $|V_2/V_1|$ and the efficiency λ versus the driving frequency for selected k_2 values, ($K_1 = 6 \times 10^{14} \text{ N/m}^3$, $K_2 = k_2 \times 6 \times 10^{14} \text{ N/m}^3$): (a) transformation ratio $|V_2/V_1|$ and; (b) efficiency λ .

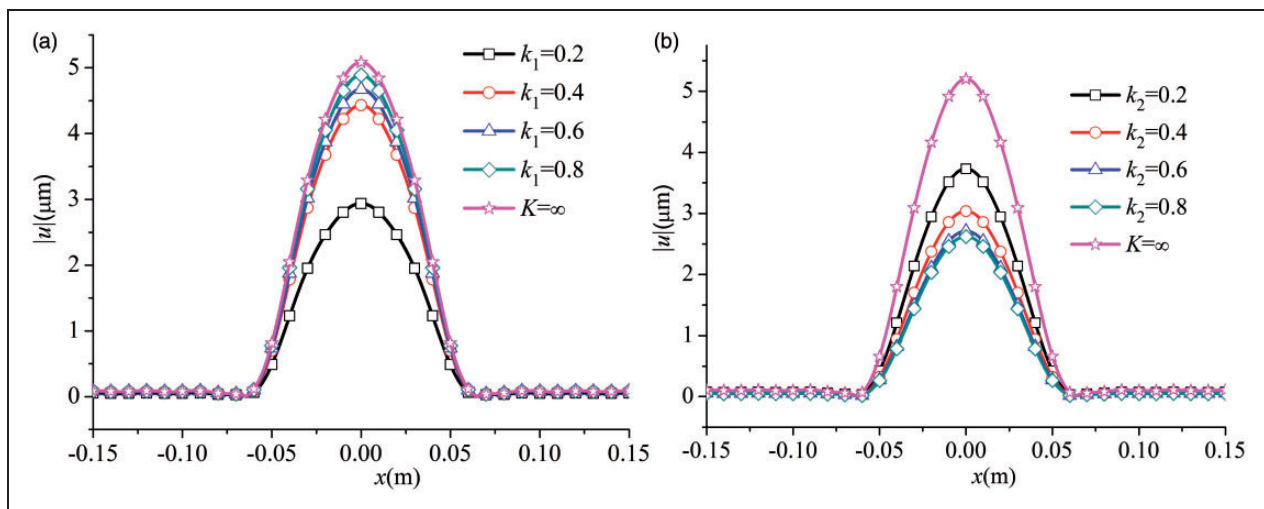


Figure 9. Displacement distribution at the first resonance for different interface situations: (a) $K_1 = k_1 \times 10^{15} \text{ N/m}^3$, $K_2 = 0.02 \times 10^{15} \text{ N/m}^3$ and (b) $K_1 = 6 \times 10^{14} \text{ N/m}^3$, $K_2 = k_2 \times 6 \times 10^{14} \text{ N/m}^3$.

guide for designing high-performance piezoelectric plate transformers.

Conflict of interest

The authors report no conflict of interest

Funding

The authors gratefully acknowledge the financial support of the work by the National Natural Science Foundation of China (grant number 11272247) and the support by grant from the Impact and Safety of Coastal Engineering Initiative, a COE Program of Zhejiang Provincial Government at Ningbo University (grant number zj1215).

References

- Auld BA (1973) *Acoustic fields and waves in solids*. New York: Wiley.
- Bao XQ, Doty BJ, Sherrit S, et al. (2007) Wireless piezoelectric acoustic-electric power feedthru. *Proceeding of SPIE: Sensors and Smart Structures Technologies for Civil, Mechanical, and Aerospace Systems* 6529: 652940.
- Cao XS, Jin F and Jeon I (2009) Rayleigh surface wave in a piezoelectric wafer with subsurface damage. *Applied Physics Letters* 95: 261906.
- Cheng ZQ, Howson WP and Williams FW (1997) Modelling of weakly bonded laminated composite plates at large deflections. *International Journal of Solids and Structures* 27: 3583–3599.

- Fan H, Yang JS and Xu LM (2006) Antiplane piezoelectric surface waves over a ceramic half-space with an imperfectly bonded layer. *IEEE Transactions Ultrasonics Ferroelectrics and Frequency Control* 53: 1695–1698.
- Fu YM, Li S and Jiang YJ (2010) Nonlinear active vibration control of piezoelectric laminated plates considering interfacial damage effects. *Journal of Vibration and Control* 16: 1287–1320.
- Handge UA (2002) Analysis of a shear-lag model with nonlinear elastic stress transfer for sequential cracking of polymer coatings. *Journal of Materials Science* 37: 4775–4782.
- He H, Liu J and Yang JS (2011) Analysis of a monolithic crystal plate acoustic wave filter. *Ultrasonics* 51: 991–996.
- Holland R and EerNisse EP (1968) *Design of resonant piezoelectric devices*. Cambridge: MIT Press.
- Hu YT, Zhang XS, Yang JS, et al. (2003) Transmitting electric energy through a metal wall by acoustic waves using piezoelectric transducers. *IEEE Transactions Ultrasonics Ferroelectrics and Frequency Control* 50: 773–781.
- Jin F, Kishimoto K, Inoue H, et al. (2005) Experimental investigation on the interface properties evaluation in piezoelectric layered structures by Love waves propagation. *Key Engineering Materials* 297: 807–812.
- Kong Y, Liu J, He H, et al. (2011) Effects of mass layer dimension on a finite quartz crystal microbalance. *Acta Mechanica* 222: 103–113.
- Lavrentyev AI and Rokhlin SI (1998) Ultrasonic spectroscopy of imperfect contact interfaces between a layer and two solids. *Journal of the Acoustical Society of America* 103: 657–664.
- Li YD and Lee KY (2010) Effect of an imperfect interface on the SH wave propagating in a cylindrical piezoelectric sensor. *Ultrasonics* 50: 473–478.
- Liu B, Jiang Q, Xie HM, et al. (2011) Energy trapping in high-frequency vibrations of piezoelectric plates with partial mass layers under lateral electric field excitation. *Ultrasonics* 51: 376–381.
- Melkumyan A and Mai YW (2008) Influence of imperfect bonding on interface waves guided by piezoelectric/piezomagnetic composites. *Philosophical Magazine* 88: 2965–2977.
- Peter BN (1992) Ultrasonic classification of imperfect interfaces. *Journal of Nondestructive Evaluation* 11: 127–139.
- Saulnier GJ, Scarton HA, Gavens AJ, et al. (2006) Through-wall communication of low-rate digital data using ultrasound. *Proceeding of IEEE Ultrasonics Symposium* 1385–1389.
- Sherrit S, Doty BJ, Badescu M, et al. (2006) Studies of acoustic-electric feed-throughs for power transmission through structures. *Proceeding of SPIE: Smart Structures and Materials* 6171: 617102.
- Wang J, Yang JS and Li JY (2007) Energy trapping of thickness-shear vibration modes of elastic plates with functionally graded materials. *IEEE Transactions Ultrasonics Ferroelectrics and Frequency Control* 54: 687–690.
- Wang YS, Yu GL, Zhang ZM, et al. (2000) Review on elastic waves propagation under complex interface (interface layer) conditions. *Advances in Mechanics* 30: 378–389 (in Chinese).
- Xu LM, Geng YL, Zhang Y, et al. (2009) Power transmission through an unbounded elastic plate using a finite piezoelectric actuator and a finite piezoelectric power harvester. *International Journal of Applied Electromagnetics and Mechanics* 29: 145–156.
- Yang JS (2005) *An introduction to the theory of piezoelectricity*. New York: Springer.
- Yang JS (2010) *Antiplane Motions of Piezoceramics and Acoustic Wave Devices*. London: World Scientific.
- Yang ZT and Guo SH (2008) Energy trapping in power transmission through a circular cylindrical elastic shell by finite piezoelectric transducers. *Ultrasonics* 48: 716–723.
- Yang ZT, Yang JS and Hu YT (2008) Energy trapping in power transmission through an elastic plate by finite piezoelectric transducers. *IEEE Transactions Ultrasonics Ferroelectrics and Frequency Control* 55: 2493–2501.
- Zhang XP, Mills JK and Cleghorn WL (2010) Experimental Implementation on vibration mode control of a moving 3_PRR flexible parallel manipulator with multiple PZT transducers. *Journal of Vibration and Control* 16: 2035–2054.